SPP1^{+}Macrophages promote the growth and metastasis of intrahepatic cholangiocarcinoma via OSM and THBS1 signaling

Short title: **SPP1^{+}**Macrophages promotes ICC progression and metastasis

Tingjie Wang[1,3*], Ruitao Long[2*], Zhongyu Cheng[2], Mi Zhang[2], Bing Wei[1,3], Cong Lyu[1,3], Cuiyun Zhang[1,3], Guangbo Tang[4], Zihang Li[5], Lei,Li[2], Yida Li[6], Xiaofei Zhu[7], Chao Shi[1,3], Ke Yang[1,3], Chuanrui Xu[2#]

*Tingjie Wang and Ruitao Long contributed equally to this work.

[1]Department of Molecular Pathology, The Affiliated Cancer Hospital of Zhengzhou University, Henan Cancer Hospital, Zhengzhou, Henan, People's Republic of China.

[2]School of Pharmacy, Tongji Medical College, Huazhong University of Science and Technology, Wuhan, China

[3]Henan Key Laboratory of Molecular Pathology, Zhengzhou, People's Republic of China.

[4]Department of Clinical Medicine Research Center, The First Affiliated Hospital of Gannan Medical University, Ganzhou, Jiangxi, People's Republic of China.

[5]Department of Hematology, The First Affiliated Hospital of Xi'an Jiaotong University, No.277 Yanta West Road, Xi'an, Shaanxi, 710061, China.

[6]Department of Chemistry & Loker Hydrocarbon Research Institute, University of Southern California, Los Angeles, California 90089, United States.

[7]Henan Key Laboratory of Immunology and Targeted Drugs, Xinxiang Key Laboratory of Tumor Microenvironment and Immunotherapy, School of Medical Technology, Xinxiang Medical University, Xinxiang, People's Republic of China.

Correspondence:

Address correspondence to: Chuanrui Xu, School of Pharmacy, Tongji Medical College, Huazhong University of Science and Technology, Wuhan, Hubei, China. Email: xcr@hust.edu.cn

Conflict of interest:

The authors declare no conflicts of interest to this work.

Abbreviations

TAMs, tumor-associated macrophages; ICC, intrahepatic cholangiocarcinoma; TME, tumor microenvironment; EMT, epithelial mesenchymal transition; Mal, malignant tumor cells region; Bdy, tumor boundary; nMal, adjacent non-malignant region; B, B cells; DC, dendritic cells; CAF, cancer-associated fibroblasts; CHO, cholangiocyte; HPE, hepatocyte; T_NK, T and NK cells; TEC, tumor endothelial cells. NEU, neutrophils. EPI, epithelial cells. BMDMs, bone marrow–derived macrophages. scRNAseq, single cell RNA sequencing; spRNAseq, spatial transcriptomics sequencing; scATACseq, single cell ATAC sequencing.

Funding:

The research was supported by grants from National Natural Science Foundation of China (82472988, 82403200, 82372667, 82273059 and 82573814), Henan Province and Ministry of Health of Medical Science and Technology Program (SBGJ202302028 for T.W. and SBGJ202402032 for C.L.), Henan Province Science and Technology Research Project (242102310051), and Henan Province Clinical Research-Oriented Physician Training Program (HNCRD202413).

Authors contributions:

C.X., T.W. designed the study. T.W., C.Z., analyzed the multi-omics data. R.L. performed experiments. T.W., R.L. wrote the manuscript. C.X. revised the article. Z.C, M.Z., C.L., B.W., L.L., X.Z. handled sample preparation. Y.L., G.T., C.S., K.Y., Z.L. managed data collection, organization. All authors read and approved the manuscript.

Data availability:

The scRNA-seq data generated in this study are available from the GEO database under accession code GSE308574. The remaining data are available within the manuscript, supplementary information, or from the corresponding author upon reasonable request.

Acknowledgements

This work was financially supported by the National Natural Science Foundation of China (Grant No. 82472988, 82403200, 82372667, 82273059 and 82573814).

Abstract

Background & Aims: Tumor-associated macrophages (TAMs) are abundant in intrahepatic cholangiocarcinoma (ICC), correlate with poor prognosis, but their spatiotemporal behavior and non-immune-suppressive roles in ICC progression remain unclear. This study sought to define transcriptional heterogeneity of TAMs and map their interactions with ICC cells that promote malignancy beyond immune suppression.

Methods: We employed three mouse ICC models, four clinical ICC patient datasets, and three spatial transcriptomic approaches to chart the macrophage landscape over time and space. Cell-cell communication analysis plus phosphoproteomics guided functional validation via TAM-ICC co-culture, cytokine treatment, gene silencing/knockout, orthotopic and metastatic ICC models, and three conditional knockout mice. A prognostic ICC tissue microarray with multiplex immunofluorescence and combinatorial blockade in mice tested efficacy of dual target inhibition. Single-cell ATAC-seq provided epigenomic profiles of TAM subsets, confirming M2 polarization networks via TCM treatment and gene silencing.

Results: In advanced ICC tissues, an M2-like subset Mφ_SPP1, defined by high expression of *SPP1*,*VEGFA*, *ARG1* and *GPNMB*, emerged as the major macrophage population, correlating with poor prognosis and spatially localizing to the tumor boundary. Further, Mφ_SPP1 drove ICC cell proliferation via the OSM-OSMR-STAT3-CCND1 and promoted invasion through THBS1-CD47-mTOR-DNB1 signalling. OSM and THBS1 were co-elevated in ICC

patient samples; dual blockade of both targets in mouse models resulted in superior inhibition of ICC progression. Lastly, MAFB directed M2 polarisation and upregulated *OSM/THBS1* in Mφ_SPP1.

Conclusions: Mφ_SPP1 TAMs accumulate at the tumor boundary in late-stage ICC, driving proliferation and invasion via *OSM* and *THBS1* signalling, underscoring the potential of macrophage-targeted therapy in ICC.

Keywords: Intrahepatic cholangiocarcinoma, Spatiotemporal omics, $SPP1^{+}$Macrophage，OSM，THBS1

Introduction

Intrahepatic cholangiocarcinoma (ICC), originating from the intrahepatic bile duct epithelium, shows rising global incidence. Its subtle early symptoms, aggressive nature, and chemotherapy resistance drive a 5-year survival rate below 10%.[1] Targeted therapies and immune checkpoint inhibitors benefit some solid tumors, but responses in ICC remain inconsistent owing to its complex tumor microenvironment (TME).[2] Tumor-associated macrophages (TAMs), the most abundant immune cells in the ICC TME, promote immune suppression, angiogenesis, and stromal remodelling,[2, 3] fuelling progression and metastasis. Current TAM-targeting strategies—depletion, reprogramming, recruitment control, and functional regulation—show variable efficacy.[4, 5] Heterogeneity is a major barrier: CD163 macrophages have low CSF-1R, reducing CSF-1R inhibitor response; CCL2 inhibitors are of limited use as CCR2 is also expressed on T and NK cells; and prolonged macrophage depletion disrupts immune homeostasis, causing adverse effects.[4] Thus, dissecting communication cascades between ICC cells and TAMS is critical to identify therapeutic targets that directly modulate ICC.

Distinct TAM phenotypes are associated with ICC progression. MARCO TAMs correlate with epithelial mesenchymal transition (EMT), angiogenesis, and hypoxia.[6] *S100P* and *SPP1*—markers distinguishing perihilar and peripheral cholangiocarcinoma—show differential macrophage infiltration tied to prognosis and grade.[7] Moreover, TAM states are highly dynamic. Prior multi-omics studies largely used patient samples, failing to track temporal polarisation across tumor stages.

Epigenetic regulation is also critically involved, but a temporal atlas of macrophage epigenetics in ICC is lacking.

Spatial distribution further influences TAM functions.[8] Spatial-omics have highlighted TAM heterogeneity.[9, 10] TAMs at invasive fronts mainly express pro-angiogenic factors such as VEGFA, while core TAMs activate immunosuppressive pathways.[6] Moreover, TAM plasticity is shaped by cues such as extracellular matrix (ECM) gradients, lactate accumulation, and cytokines.[9] However, the spatial dynamics of TAMs in ICC remain poorly defined.

Here, we developed a temporal ICC mouse model, tracked TAM evolution, and identified shared human subpopulations, mapping their transcriptional and regulatory landscapes. Using cell-cell communication analysis, co-culture, multiplex immunofluorescence, and knockout models, we validated key TAM factors in ICC progression. These findings are expected to support macrophage-targeted immunotherapy for ICC.

Materials and methods

Animal Models：

Wild-type FVB and C57BL/6 mice were purchased from Beijing Vital River Laboratory Animal Technology Co., Ltd. (Beijing, China). Genetically modified mice were provided by Shulaibao (Wuhan) Biotechnology Co., Ltd. (Wuhan, China). All laboratory mice were kept in a specific pathogen-free (SPF) environment. Experimental protocols involving animals were approved by the Ethics Committee of Huazhong University of Science and Technology. Detailed information on the animals used in this study is provided in Supplementary Table S1.

Cell source

The human cholangiocarcinoma cell lines HuCCT1, RBE, and QBC939, as well as the mouse fibroblast cell line L929 and macrophage cell line RAW 264.7, were used in this study. HuCCT1 was obtained from the Japanese Collection of Research Bioresources Cell Bank (JCRB, Osaka, Japan; accession number JCRB0425). RBE was acquired from the China Center for Type Culture Collection (CCTCC, Wuhan, China; accession number GDC0765). QBC939 was purchased from Shanghai Jinyuan Biological Technology Co., Ltd (Shanghai, China; product code JY-Y1457). The mouse cell lines L929 (ATCC® CCL-1™) and RAW 264.7 (ATCC® TIB-71™) were purchased directly from the American Type Culture Collection (ATCC, Manassas, VA, USA). All cells were cultured according to the providers' recommendations and were routinely tested to be free of mycoplasma contamination.

BR cells, isolated from BMI1/NRAS-driven orthotopic tumor models in FVB mice, were maintained in RPMI-1640 complete medium supplemented with 10% FBS and 1% penicillin–streptomycin at 37°C with 5% CO_2 in an incubator. These cells displayed consistent in vitro growth characteristics and were capable of forming tumors in both subcutaneous and orthotopic liver implantation models in wild-type FVB mice. Immunohistochemistry (IHC) and histopathological analysis confirmed the presence

of ICC features.

Establishment of the ICC mouse model

Hydrodynamic tail vein injection was performed in 6 – 8 weeks mice to establish primary ICC mouse models. For AKT1/NICD1 ICC mouse model , a mixture of plasmids, including 15 μg pT3-EF1aH-myr-AKT, 15 μg pT3-EF1a-NICD1, and 1.5 μg pCMV-SB, was diluted in 2 mL of sterile saline and filtered through a 0.22 μm membrane to remove impurities. For AKT1/YAP1 ICC mouse model, a mixture of plasmids, including 15 μg pT3-EF1aH-myr-AKT, 15 μg pT3EF1αH-YAPS127A, and 1.5 μg pCMV-SB, was diluted in 2 mL of sterile saline. For sgP19/KRAS high-metastasis ICC model, a mixture of plasmids, including 10 μg CRISPR-Cas9-sgP19, 25 μg pT3-EF1α-KRAS, and 5.0 μg pCMV-SB, was diluted in 2 mL of sterile saline. The injection volume for a 20 g mouse was 2 mL and adjusted according to body weight in proportion. Mice were restrained on a tail vein visualization platform, and the injection was completed within 5 – 7 seconds. Mice were euthanized and dissected upon reaching predefined tumor endpoint criteria.

The plasmids were generously provided by Dr. Chen Xin (University of Hawai□i Cancer Center). Bacterial cultures were grown in LB medium containing 100 μg/mL ampicillin at 37°C with shaking at 180 rpm for 12 hours, followed by plasmid extraction using the Omega plasmid purification kit.

Multi-omics analyses and bioinformatic analysis

scRNA-seq, spatial transcriptomics, scATAC-seq, phosphoproteomics were performed. Detailed methods are provided in the Supplementary Methods.

Results

Mφ_SPP1 is dominant at the ICC boundary and linked to poor prognosis

To dissect macrophage subsets driving ICC malignancy, we established an AKT1/NICD1 induced ICC mouse model via hydrodynamic tail vein injection and collected liver tissue at day 7 (early ICC), day 15 (mid ICC), day 25 (mid/advanced ICC), and day 31 (advanced ICC). Single cell RNA sequencing (scRNAseq) was performed at all stages and spatial transcriptomics sequencing (spRNAseq) was performed at day 31, with integrated analysis of public human datasets (Table S2, Fig. S1A-F).

Four conserved TAM subsets were identified in mouse and human ICC: Mφ_CXCL9(human)/Mφ_Cxcl9(mouse),Mφ_S100A/Mφ_S100a,Mφ_C1QA/Mφ_C1qa, and Mφ_SPP1/Mφ_SPP1 (Fig. 1A-B, S1, Table S2). Mφ_Cxcl9 and Mφ_S100a dominated early/mid-stage mouse ICC (Fig. 1B), while in humans, Mφ_CXCL9 localised to adjacent liver and elevated expression of *CXCL9*, *CXCL11*, and *CCL5* (Fig. S1C, S1G), while Mφ_S100A was enriched in human ICC tissues with elevated *CD68*, *VCAN*, *S100A4*, *S100A8* (Fig. 1C, S1C, S1G), suggesting an inflammatory early ICC microenvironment. In contrast, Mφ_C1QA/Mφ_C1qa and Mφ_SPP1/Mφ_SPP1 were enriched in human ICC and advanced mouse ICC, with similar transcriptional signatures (Fig 1C). Mφ_SPP1 showed elevated *GPNMB*, *VEGFA*, *ARG1*, *APOE*, *TREM2*, and *SPP1* levels (Fig 1C，S1C, S1G), consistent with M2-like, tumor-promoting macrophages.[11, 12] Mφ_SPP1 showed significant enrichment in cytokine secretion and tumor proliferation pathways (Fig. S1H). Similar

TAM subtypes and temporal patterns were confirmed in AKT1/YAP1 ICC mice (Figure S2A–C). Kupffer cells (*Clec4f*$^{+}$*Mrc1*$^{+}$ *and Vegfa*/*Gpnmb*/*Spp1*-low), were abundant in AKT1/NICD1 and AKT1/YAP1 ICC tissues, likely from liver damage caused by hydrodynamic injection (Fig. 1C, S1G, S2A–D).

Analysis of dynamic macrophage temporal distribution using pseudo-time analysis showed that Mφ_Cxcl9 andMφ_S100a predominated the early pseudo-time branch, while Mφ_SPP1 progressively expanded in later branches (Fig 1D, S2E), indicating that Mφ_SPP1 is the dominant population in advanced ICC tissues. Prognostic analysis across three independent cohorts (GSE89749,[13] GSE107943,[14] GSE244807[15]) confirmed the robust association of Mφ_SPP1 with poor outcome of patients with ICC (Fig. 1E, S2F).

In mouse ICC allografts, established by co-injection of BMDMs with BR ICC cells, tumor growth was significantly enhanced by macrophages, characterised by F4/80□ and CD206□ (Fig. 1F-i, S3), while depletion of macrophages using clodronate liposome (Fig. S4) suppressed tumor progression (CD11b□F4/80□/CD45□), evidenced by increased liver-to-body weight ratio (Fig. 1F-ii). Co-culture of ICC cells with macrophages caused M2-like polarisation of macrophages, with robust upregulation of M2 polarisation markers including *ARG1*, *VEGFA*, *IL10*, and *MRC1* (Fig. S5), using non-contact Transwell co-cultures or treatment with tumor-conditioned medium (TCM)(Fig. S5B-D). In Transwell co-culture systems, EdU incorporation assay and migration assay demonstrated that macrophage co-culture significantly enhanced ICC cell proliferation (Fig. S6A-D) and

migration (Fig. S6E).

Next, utilizing three spatial transcriptomics platforms and multiplex immunofluorescence, we explored the spatial distribution of Mφ_Spp1 and its spatial proximity to ICC cells across one public dataset[16] and four in-house ICC datasets (Table S2). In the public human ICC dataset with the 10X Visium platform, we observed that spatial clusters C0 and C4, located in the non-malignant region (nMal), exhibited a high infiltration of hepatocytes (HPE) (Fig. 1G(i-ii)). In contrast, in the malignant (Mal) and boundary (Bdy) regions, clusters C1, C2, and C3 were enriched in ICC cells and $SPP1^+$ macrophages (Fig. 1Gii-iii, S7). Simultaneously, we performed tumor niche analysis and confirmed the co-occurrence of $CK19^+$ epithelial and macrophage cells (Fig. 1G-iv). Additionally, in the high-resolution spatial transcriptome analysis of D31 AKT1/NICD1 ICC tissue using the BMKMANU S1000 platform, we identified that the Mφ_Spp1 subtype was predominantly localized to the tumor boundary, adjacent to $CK19^+$ ICC cells within the same tumor niche (Fig. 1H, S7). Similarly, in the in-house 10X HD transcriptome data from four human ICC tissues, we conducted spatial domain analysis using BANKSY and RCTD, further validating the spatial proximity between Mφ_SPP1 and $CK7^+CK19^+$ ICC cells (Fig. 1I i-iv). Specifically, we assessed whether the abundance of ICC cells could be predicted by their spatially adjacent TME cells using mistyR in ICC patient #1. We found that Mφ_Spp1 cells were the most predictive of the abundance of $CK7^+CK19^+$ ICC cells (Fig. 1I (v)), a finding also corroborated in the other three patients (Fig. S7D-E). We also validated the spatial proximity between $SPP1^+CD68^+$ and $CK19^+$

cells in the other two ICC patient cohorts using multiplex immunofluorescence (mIF) (Fig. 1J). The results showed that SPP1^{+} CD68^{+} macrophages were highly enriched in the periphery of CK19^{+} cells (0–20 μm), and their abundance gradually diminished with increasing spatial distance(Fig. 1J).

Together, these findings indicate that M2-like Mφ_SPP1 accumulate at the ICC boundary, driving proliferation and invasion through cytokine secretion.

Mφ_SPP1 promotes ICC proliferation via the OSM-OSMR-STAT3-CCND1 axis

To explore the mechanisms underlying Mφ_SPP1-mediated ICC progression, we re-clustered and obtained seven epithelial cell subpopulations from human and AKT1/NICD1 mouse ICC. Within human/mouse shared subtypes, E_Alb in mice or E_ALB in human were normal hepatic epithelial cells with high *ALB* levels (Fig. 2A, 2B, S8A). E_Fxyd2 (mouse) or E_FXYD2 (human) were normal cholangiocytes with high *FXYD2* levels (Fig. 2A, 2B, S8A). In contrast, E_Jun/E_Spp1 (mouse) and E_CD74/E_IGFBP7 (human) showed high CNV scores (Fig. S8B) and were identified as ICC cells. Specifically, E_Jun (mouse)/E_Cd74 (human) displayed high expressions of *STAT3*, *JUN*, *HSPA1A* and *CCND1* (Fig. 2A, S8A), indicating their stress-responsive and highly proliferative nature.[17, 18] Meanwhile, E_Jun/E_Spp1 (mouse) and E_IGFBP7 (human) exhibited high levels of the EMT-related genes *VIM*, *COL4A1*, and *FN1* (Fig. 2A, S8A). In addition, E_Mki67 (mouse)/E_MKI67 (human) displayed high expressions of MKI67 but low expressions of receptor genes.

Integration of three cell-cell communication approaches (CellChat, CellphoneDB, NicheNet) to analyse interactions between Mφ_SPP1 and ICC cells with high

proliferation and EMT features and the downstream signalling pathways, revealed that Mφ_SPP1 engages with ICC cells via *OSM* and *THBS1* ligands (Fig. 2C–D). *OSM*, enriched in Mφ_Spp1 (mouse) and Mφ_SPP1 (human), interacted with ICC cells of E_Jun in mice and E_CD74 in human via *OSMR* and *LIFR*, which in turn activated the genes involved in cytokine response and epithelial proliferation (Fig. 2E, S8C–D).

To test whether *OSMR* and *LIFR* are required for ICC progression, we generated *Osmr*- or *Lifr*- liver conditional knockout mice Osmr$^{fl/fl}$;Alb-cre and Lifr$^{fl/fl}$;Alb-cre, followed by hydrodynamic injection of AKT1/NICD1 via tail vein. Compared with Lifr $^{fl/fl}$ mice, Lifr $^{fl/fl}$; Alb-Cre mice showed no significant difference in liver-to-body weight ratio upon AKT1/NICD1 injection (Fig. 2F–G, S9A-B). However, Osmr $^{fl/fl}$;Alb-Cre mice exhibited a marked reduction of liver-to-body weight ratio after AKT1/NICD1 injection compared to Osmr $^{fl/fl}$ mice (Fig. 2F–G, S9A-B). qRT-PCR revealed that *Osm* and *Osmr* levels increased with tumor progression (Fig. S9C). Spatial interaction analysis (Fig. S10A-B), expression level in ICC scRNAseq cohorts (GSE210066 and GSE201425, Table S2, Fig. S10C), and spatial mapping by multiplex IF (Fig. 2H, S10G) all confirmed the presence of OSM□ macrophages in the vicinity of OSMR□ tumor cells.

Functionally, RAW264.7 and QBC939 co-cultures increased *OSM*, *VEGFA*, and *IL10* in macrophages, and *OSMR* in QBC939 cells (Fig. 3A, S11A). Similarly, co-culture with BMDMs increased OSMR protein levels in BR cells (Fig. S3B-i). Recombinant OSM increased OSMR mRNA and protein levels, and viability of ICC

cells (Fig. 3B). OSMR knockdown (siRNA) significantly suppressed ICC cell viability (Fig. S11C-D). Similarly, CRISPR-Cas9-mediated knockout of *OSMR* resulted in significantly decreased proliferation, viability, and clonogenicity of ICC cells (Fig. 3C, S11E).

Phosphoproteomics of QBC939 cells treated with recombinant OSM revealed enrichment of PI3K-AKT, MAPK, and cell cycle-related pathways (Fig. 3D). Moreover, *Osmr* in the tumor subtype E_Jun was involved in epithelial cell proliferation, cytokine response, and MAPK pathways, and interacted with *Stat3* and *Ccnd1* (Fig. 3E). Thus, OSM-OSMR may activate STAT3-CCND1 signalling in tumor cells. To test this hypothesis, we used $Osmr^{fl/fl}$;Alb-Cre mice injected with AKT1/NICD1. H&E and IHC staining demonstrated that ICC lesions formed in $Osmr^{fl/fl}$;Alb-Cre mice were significantly smaller than those in $Osmr^{fl/fl}$ mice (Fig. 3F, S12A). The tumor-suppressive effect of *Osmr* knockout was similarly validated in a hydrodynamic injection-constructed AKT1/YAP1 ICC mouse model, manifesting as significantly reduced liver-to-body weight ratio and diminished tumor nodule formation (Fig S12B, C). Notably, *Osmr* knockout did not alter F4/80□ and CD206□ macrophage infiltration levels (Fig. S12D). However, the levels of the downstream proteins CCND1, BCL2, and p-STAT3 were markedly reduced (Fig. 3G), indicating that Mφ_SPP1 promotes ICC growth via OSM-OSMR signalling and downstream STAT3 phosphorylation, suggesting that deficiency of OSM-OSMR signalling leads to retarded ICC growth in mice.

Mφ_SPP1 TAMs promote ICC invasion through the *THBS1-CD47-mTOR-DBN1* axis

In addition to *OSM*, *THBS1* is secreted by Mφ_SPP1 which may promote ICC development. Cell communication analysis showed that *THBS1* interacted with E_Jun and E_Spp1 in AKT1/NICD mouse ICC tissues and with E_IGFBP7 in human ICC via *CD47* (Fig. 4A, Fig. S13A). Using NicheNet, we found that *THBS1*-regulated target genes in ICC cells were mainly enriched in EMT-related signalling (Fig. 4B, S13B). Subsequently, we validated the THBS1-CD47 interaction both in vitro and in vivo. In vitro, recombinant THBS1 exhibited moderate growth-promoting and enhanced pro-migratory effects in ICC cells (Fig. S14A, B). Specifically, treatment with 10 ng/mL recombinant THBS1 significantly enhanced wound-healing (Fig. 4C) and migration of ICC cells (Fig. 4D). Correspondingly, *CD47* silencing significantly impaired the stimulatory effects of THBS1 in promoting ICC cell migration (Fig. 4E–F, Fig. S14C, D). Stable knockdown of *Cd47* in BR cells significantly inhibited the proliferation, colony formation capability and viability of ICC cells (Fig. 4G–J). Co-culture with BMDMs promoted BR migration ability, whereas *Cd47* knockdown blocked this effect (Fig. 4K). Similarly, *Cd47* silencing inhibited subcutaneous allograft growth in mice (Fig. 4L, Fig. S14E, F). Moreover, *Cd47* knockdown markedly suppressed ICC dissemination in a peritoneal metastasis mouse model, as evidenced by reduced metastatic nodule formation and decreased ascites accumulation (Fig. 4M(i-ii), Fig. S14G, H). Consistently, CD47 silencing attenuated ICC growth and local invasion into the surrounding hepatic parenchyma in the

primary ICC mouse model (Fig. 4M-iii).

To elucidate the role of *THBS1*-mediated EMT in ICC, we performed western blotting, which revealed that recombinant THBS1 induced rapid induction of EMT-related proteins at 10 min with a peak at 2 h, accompanied with increased levels of p-mTORC1 and downstream p-RPS6 (Fig. 5A, S15A). Phosphoproteomic analysis of HuCCT1 cells treated with recombinant THBS1 at 0, 2, and 12 h revealed elevated phosphorylation of PI3K-AKT and EMT-related signalling proteins at 2 h (Fig. 5B). In comparison, differential protein phosphorylation was enriched in cell adhesion and RNA metabolism pathways at 12 h (Fig. 5B, S15B). Specifically, ranking differentially phosphorylated sites by fold change (2 h vs 0 h) identified DBN1 Ser142 as the most strongly upregulated phosphorylation site at 2 h (Fig. 5C).

Co-culture of ICC cells with BMDM led to increased *Arg1*, *Vegfa*, and *Thbs1* in BMDMs, CD47, p-mTORC1, p-DBN1 and Vimentin in ICC cell lines (Fig. 5D, Fig. S16A–B). The upregulation of *Thbs1* and *Cd47* was also detected by qRT-PCR in AKT1/NICD1-induced liver tissues (Fig. S16C–D). Inhibition of mTORC1 by rapamycin substantially suppressed the pro-migratory effect of BMDMs on ICC cells (Fig. 5E) and completely abrogated the THBS1-induced migration (Fig. 5F), indicating that THBS1 promotes ICC cell migration via mTORC1 activation. Meanwhile, inhibition of DBN1 via its inhibitor BTP2 significantly blocked the migration of ICC cells (Fig. 5G). Notably, BTP2 exerted its inhibitory effect by decreasing phosphorylation at Ser142 of DBN1 (Fig. S16 E). Together, these results demonstrate the critical roles of p-mTORC1 and DBN1 Ser142 phosphorylation in the

THBS1-mediated migration signalling pathway.

Finally, we examined the role of THBS1 in ICC progression by combing a highly metastatic sgP19/KRAS ICC model with Thbs1$^{fl/fl}$;Lyz-Cre mice (Fig. 5I). Myeloid-specific konckout of *Thbs1* significantly reduced liver-to-body weight ratios and tumor burden, while also markedly suppressing peripheral metastasis to multiple distant organs - including the intestines, lungs, lymph nodes, kidneys and diaphragm (Fig. 5H-J , FigS16F). Notably, THBS1 knockout also demonstrated significant efficacy in suppressing ICC within the AKT1/NICD1 model—which lacks prominent peripheral metastasis (Fig.5 K, L). This finding underscores the crucial contribution of local intrahepatic spread to ICC progression. Furthermore, Western blotting of ICC tissues revealed that metastasis related CD47, DBN1, p-DBN1, p-mTORC1, and Vimentin levels were significantly downregulated after *Thbs1* deletion (Fig. 5M). Collectively, these findings corroborate that THBS1 promotes ICC metastasis via PI3K-AKT-mTOR activation and DBN1 phosphorylation.

Combined blockade of OSM and THBS1 effectively inhibits ICC progression

Since *OSM* promotes proliferation and *THBS1* enhances invasiveness, we asked whether dual inhibition could synergistically suppress ICC. We analysed *THBS1* and *OSM* expression in 833 patients from 9 ICC/Cholangiocarcinoma cohorts (Table S2), and calculated the mean expression levels of *THBS1* and *OSM* in each cohort. An ICC sample was defined as double-positive if both genes had expression levels greater than the mean value of the cohort. Using this criterion across 9 datasets, the

proportion of *THBS1/OSM* double-positive ICC samples ranged from 13.33% to 29.53%, and exceeded 20% in five datasets (Fig. 6A). Prognostic analyses across three datasets showed that patients with high expression of both OSM and THBS1 had significantly shorter overall survival (OS) (Fig. 6B). Next, we genetically ablated macrophage-derived *THBS1* using Thbs1$^{fl/fl}$; Lyz-cre mice and pharmacologically inhibited OSM-OSMR interaction via intraperitoneal administration of OSM-SMI-10B, an OSMR inhibitor.[19] *Thbs1* deletion or *Osmr* inhibition alone suppressed ICC progression moderately, while combined blockade attenuated ICC development more robustly, as evidenced by further reduced tumor burden using H&E staining and a decreased liver-to-body weight ratio (Fig. 6C–E). These results collectively indicate that combined blockade of OSM and THBS1 may generate synergetic therapeutic effects for ICC treatment. Finally, we validated the spatial proximity relationship between OSM/THBS1 and CK19 cells using mIF (Fig. 6F). The results showed that OSM^{+}THBS1^{+}CD68^{+} cells were spatially adjacent to CK19^{+} cells (Fig. 6F i-ii), OSM and THBS1 were co-expressed in CD68^{+} cells (Fig. 6F-iii). Patients with high OSM/THBS1 co-expression was associated with significantly worse survival (Fig. 6F-iv). These findings suggest that macrophage-derived OSM and THBS1 represent promising therapeutic targets in a substantial subset of ICC patients.

Mafb promotes M2 polarisation and enhances *OSM* and *THBS1* expression in macrophages

We next examined epigenetic modification in macrophages. Liver tissues from

AKT1/NICD1 ICC mice at middle/advanced stages and vector controls were subjected to time-series single cell ATAC sequencing (scATAC-seq) to map regulatory elements in Mφ_SPP1 (Fig. S17A–C). Accessibility profile analysis of cell type markers using ArchR (V1.0.3) and integrated AKT1/NICD1 scRNA-seq and scATACseq data identified seven major cell types (CAF, TEC, EPI, B, NEU, T_NK, and TAMs; Fig. 7A, S17A–B). Further, re-clustering of TAMs revealed three subtypes—Mφ_Clec4f, Mφ_Spp1, and Mφ_S100a (Fig. 7A, S17C). ArchR to analyze chromatin accessibility and transcription factor (TF) motifs across TAM subtypes revealed that Mφ_Spp1 and Mφ_S100a subsets exhibited markedly distinct regulatory landscapes (Fig. 7B). In Mφ_S100a, the Klf transcription factor family exhibited specific activation (Fig 7B, S17D), with TF *Klf3* showing the highest expression and regulating inflammation response genes including *S100a4* and *S100a8* (Fig. 7C, 7D, S17D, S17E). In comparison, Mφ_Spp1 displayed preferential chromatin accessibility of *Maf* transcription factor family (Fig 7B), with *Mafb* showing the highest expression (Fig. 7C). Notably, *Mafb* regulated genes were enriched in cell differentiation pathways—*Mafb* was predicted to regulate M2 polarisation markers (*Cd163*, *Mrc1*, *Il10*) and *Osm* (Fig. 7D, S17F). *MAFB* was highly expressed at the tumor boundary in mouse and human ICC tissues (Fig. 7E). *Mafb* also showed significantly increased chromatin accessibility in Mφ_Clec4f (Kupffer cells). Mφ_Clec4f exhibited high accessibility of *Cd163* and *Mrc1* but low expression of *Osm* and *Thbs1* (Fig. S17G), indicating that the regulatory role of *Mafb* on *Osm/Thbs1* is specific to Mφ_Spp1. Together, these data suggest that *Mafb* plays an important role in regulating

macrophage M2 polarisation.

To validate the role of Mafb in Mφ_Spp1, we combined macrophage pseudotime analysis with immune infiltration profiling to identify key signals driving macrophage polarization (Fig. S18). Pseudotime-associated genes were grouped into five clusters, among which cluster 4 was enriched for mononuclear cell differentiation (Fig. S18A–B). We then selected genes with an average expression > 1 in Mφ_Spp1 and a positive correlation with M2 polarization (r > 0.5) in the TCGA-CHOL cohort using TIMER2.0, yielding eight candidates, including the transcription factor *MAFB* and the receptor *TGFBR2* (Fig. S18C–D).

We next performed cell–cell communication analysis between ICC cells and TAM subtypes in the AKT1/NICD1 dataset, and found that the E_Jun ICC subcluster interacts with Mφ_Spp1 via the Tgfb2–Tgfbr2 ligand–receptor pair (Fig. S18E–F). In the Transwell co-culture system, *TGFB2* was upregulated in ICC cells, while *Tgfbr2* was upregulated in BMDMs (Fig. S19A). As TGF-β2 has also been reported to regulated M2 polarisation,[20] We found that TCM or recombinant TGF-β2 significantly upregulated the expression of M2 markers in BMDMs, including *Mrc1* (Cd206), *Arg1*, and *Mafb*-regulated genes *Tgfbr2*, *Thbs1*, and *Osm* (Fig 7F, 7G, Fig S19B, C). Crucially, siRNA knockdown of *Mafb* significantly reduced expression of *Arg1*, *Vegfa*, *Osm*, and *Thbs1* (Fig. 7H). These results indicate that *MAFB* could regulate macrophage M2 polarisation via *OSM* and *THBS1* signalling.

Discussion

The roles of TAMs in ICC have been linked to poor prognosis through promotion of tumor growth and invasiveness.[21, 22] Recent single-cell omics studies have revealed the molecular diversity and functions of TAMs in cancer,[23] but the specific subgroups driving ICC malignancy and its interactions with tumor cells remain unclear. Using a time-resolved ICC mouse model with integrated multi-omics, we identified Mφ_SPP1 as a poor-prognosis TAM subset in ICC. Spatial transcriptomics confirmed its boundary localisation and functional niche. Mφ_SPP1 displayed mainly M2-like traits with distinct marker genes separating it from other TAMs. Its prognostic significance was also observed in hepatocellular carcinoma (HCC),[11] underscoring relevance across liver cancer, highlighting Mφ_SPP1 as a therapeutic target for both ICC and HCC.[24] Mechanistically, Mφ_SPP1 promotes ICC proliferation and invasion through coordinated multiple pathway via OSM-OSMR signalling, activating STAT3 phosphorylation and CCND1 induction, similar to glioblastoma [25] This observation is consistent with the finding that OSM promotes cancer cell proliferation and differentiation in breast cancer and pancreatic ductal adenocarcinoma.[26] Its pro-invasive function depends on the secreted matricellular glycoprotein THBS1, which activates CD47 signalling in ICC cells. THBS1 derived from tumor-infiltrating monocyte-like cells reportedly induces an immunosuppressive TME and contributes to cancer metastasis.[27] Notably, we demonstrate that *CD47* activates mTOR in ICC cells but not IL6/STAT3, resulting in DBN1 Ser124 phosphorylation, as also observed

in oral squamous cell carcinoma.[28] While THBS1/CD47 mediate immune evasion, our study reveals its direct role in ICC proliferation and invasion.

Our findings offer a new therapeutic strategy for ICC treatment aiming at macrophages. OSM/OSMR and THBS1/CD47 axes mediate macrophage-ICC interactions, suggesting their potential as therapeutic targets for ICC. Although administration of single OSM or mTOR inhibitors (blocking CD47 signalling) achieved limited inhibitory effect on ICC growth, combined blockade of OSM-OSMR and THBS1/CD47 signalling generated synergetic anti-tumor effects in an ICC mouse model. Consistently, a clinical trial showed that targeting OSM/OSMR signalling alone led to poor outcome or drug resistance.[29] Thus, targeting dual modulators of Mφ_SPP1 provides a potentially more robust therapeutic option. Further, OSM and THBS1 were concurrently upregulated in 13–29% of patients with ICC and OSM/OSMR and THBS1/CD47 signalling promoted ICC proliferation and migration, respectively. Therefore, combination therapy targeting these two signalling pathways may be effective in patients with ICC at different stages.

Lastly, our study indicates that Mφ_SPP1 polarisation is dependent on MafB and demonstrates a metabolic profile with highly active lipid metabolism. MafB has been reported with c-Maf functioning as a self-renewal blocker in monocytes and macrophages, and deficiency of these two genes enables extended expansion of mature monocytes and macrophages in culture while maintaining their differentiated phenotype and function.[30] In addition, macrophages express acute inflammatory

response genes in a Maf-dependent manner upon bacteria exposure and simultaneously downregulate Maf through accelerated degradation via the proteasome pathway and microRNA-mediated silencing.[31] In this study, we further demonstrate that MAF is required for macrophage polarisation in the TME and highlight the roles of MAF in orchestrating macrophage activation and polarisation.

Supplementary Material

Note: To access the supplementary material accompanying this article, visit the online version of *Gastroenterology* at www.gastrojournal.org,

References

[1] Moris D, Palta M, Kim C, et al. Advances in the treatment of intrahepatic cholangiocarcinoma: An overview of the current and future therapeutic landscape for clinicians. CA: a cancer journal for clinicians 2023;73:198-222. https://doi.org/10.3322/caac.21759.

[2] Greten TF, Schwabe R, Bardeesy N, et al. Immunology and immunotherapy of cholangiocarcinoma. Nat Rev Gastroenterol Hepatol 2023;20:349-365. https://doi.org/10.1038/s41575-022-00741-4.

[3] Zhou M, Wang C, Lu S, et al. Tumor-associated macrophages in cholangiocarcinoma: complex interplay and potential therapeutic target. EBioMedicine 2021;67:103375. https://doi.org/10.1016/j.ebiom.2021.103375.

[4] Guan F, Wang R, Yi Z, et al. Tissue macrophages: origin, heterogenity, biological functions, diseases and therapeutic targets. Signal Transduct Target Ther 2025;10:93. https://doi.org/10.1038/s41392-025-02124-y.

[5] Chen S, Saeed A, Liu Q, et al. Macrophages in immunoregulation and therapeutics. Signal Transduct Target Ther 2023;8:207. https://doi.org/10.1038/s41392-023-01452-1.

[6] Fan G, Tao C, Li L, et al. The co-location of MARCO+ tumor-associated macrophages and CTSE+ tumor cells determined the poor prognosis in intrahepatic cholangiocarcinoma. Hepatology 2025;82:25-41. https://doi.org/10.1097/HEP.0000000000001138.

[7] Song G, Shi Y, Meng L, et al. Single-cell transcriptomic analysis suggests two molecularly subtypes of intrahepatic cholangiocarcinoma. Nat Commun 2022;13:1642. https://doi.org/10.1038/s41467-022-29164-0.

[8] Li Z, Li Zhao, Chen Q, et al. Single-Cell and Spatial Transcriptomics Delineate the Microstructure and Immune Landscape of Intrahepatic Cholangiocarcinoma in the Leading-Edge Area. Ad Sci 2025;12:e2412740. https://doi.org/10.1002/advs.202412740.

[9] Yan J, Jiang Z, Zhang S, et al. Spatial□temporal heterogeneities of liver cancer and the discovery of the invasive zone. Clin Transl Med 2025;15:e70224. https://doi.org/10.1002/ctm2.70224.

[10] Dong LQ, Shi Y, Ma LJ, et al. Spatial and temporal clonal evolution of intrahepatic cholangiocarcinoma. J Hepatol 2018;69:89-98. https://doi.org/10.1016/j.jhep.2018.02.029.

[11] Zhang Q, He Y, Luo N, et al. Landscape and Dynamics of Single Immune Cells in Hepatocellular Carcinoma. Cell 2019;179:829-845.e820. https://doi.org/10.1016/j.cell.2019.10.003.

[12] Su X, Liang C, Chen R, et al. Deciphering tumor microenvironment: CXCL9 and SPP1 as crucial determinants of tumor-associated macrophage polarity and prognostic indicators. Mol Cancer 2024;23:13. https://doi.org/10.1186/s12943-023-01931-7.

[13] Jusakul A, Cutcutache I, Yong CH, et al. Whole-Genome and Epigenomic Landscapes of Etiologically Distinct Subtypes of Cholangiocarcinoma. Cancer Discov 2017;7:1116-1135. https://doi.org/10.1158/2159-8290.CD-17-0368.

[14] Ahn KS, O'Brien D, Kang YN, et al. Prognostic subclass of intrahepatic cholangiocarcinoma by integrative molecular-clinical analysis and potential targeted approach. Hepatol Int 2019;13:490-500. https://doi.org/10.1007/s12072-019-09954-3.

[15] Lubuela G, Beaufrere A, Albuquerque M, et al. Prognostic impact of the tumor microenvironment in intrahepatic cholangiocarcinoma: identification of a peritumoral fibro-immune interface. Virchows Arch 2024;485:901-911. https://doi.org/10.1007/s00428-024-03922-5.

[16] Wu R, Guo W, Qiu X, et al. Comprehensive analysis of spatial architecture in primary liver cancer. Sci Adv 2021;7:eabg3750. https://doi.org/10.1126/sciadv.abg3750.

[17] Low J, Altman R, Badolian A, et al. Heat-induced phosphatidylserine changes drive HSPA1A's plasma membrane localization. Cell Stress Chaperones 2025;30. https://doi.org/10.1016/j.cstres.2025.100092.

[18] Shashikanth N, Alaidi O, Basa L, et al. Role of C-Jun N-Terminal Kinases on a Stressed Epithelium: Time for Testing Isoform Specificity. Biology 2025;14:649. https://doi.org/10.3390/biology14060649.

[19] Wolf CL, Feci A, Tuccinardi JP, et al. Development of the First Small-Molecule Inhibitor Targeting Oncostatin M for Treatment of Breast Cancer. J Med Chem 2025;68:15422-15445. https://doi.org/10.1021/acs.jmedchem.4c03233

[20] Luo L, Wang S, Hu Y, et al. Precisely Regulating M2 Subtype Macrophages for Renal Fibrosis Resolution. ACS Nano 2023;17:22508-22526. https://doi.org/10.1021/acsnano.3c05998.

[21] Hasita H, Komohara Y, Okabe H, et al. Significance of alternatively activated macrophages in patients with intrahepatic cholangiocarcinoma. Cancer Sci 2010;101:1913-1919. https://doi.org/10.1111/j.1349-7006.2010.01614.x.

[22] Hui Y, Lin Z, Liu Y, et al. Intrahepatic cholangiocarcinoma induced M2-polarized tumor-associated macrophages facilitate tumor growth and invasiveness. Cancer Cell Int 2020;20:586. https://doi.org/10.1186/s12935-020-01687-w.

[23] Ma RY, Black A, Qian BZ. Macrophage diversity in cancer revisited in the era of single-cell omics. Trends Immunol 2022;43:546-563. https://doi.org/10.1016/j.it.2022.04.008.

[24] Okikawa S, Morine Y, Saito Y, et al. Inhibition of the VEGF signaling pathway attenuates tumor□associated macrophage activity in liver cancer. Oncol Rep 2022;47:71. https://doi.org/10.3892/or.2022.8282.

[25] Chen M, Ren R, Lin W, et al Exploring the oncostatin M (OSM) feed-forward signaling of glioblastoma via STAT3 in pan-cancer analysis. Cancer Cell Int 2021;21:565. https://doi.org/10.1186/s12935-021-02260-9.

[26] Polak KL, Tamagno I, Parameswaran N, et al. Oncostatin-M and OSM-Receptor Feed-Forward Activation of MAPK Induces Separable Stem-like and Mesenchymal Programs. Mol Cancer Res 2023;21:975-990. https://doi.org/10.1158/1541-7786.MCR-22-0715.

[27] Omatsu M, Nakanishi Y, Iwane K, et al. THBS1-producing tumor-infiltrating monocyte-like cells contribute to immunosuppression and metastasis in colorectal cancer. Nat Commun 2023;14:5534. https://doi.org/10.1038/s41467-023-41095-y.

[28] You Y, Tian Z, Du Z, et al. M1-like tumor-associated macrophages cascade a mesenchymal/stem-like phenotype of oral squamous cell carcinoma via the IL6/Stat3/THBS1 feedback loop. J Exp Clin Cancer Res 2022;41:10. https://doi.org/10.1186/s13046-021-02222-z.

[29] Wolf CL, Pruett C, Lighter D, et al. The clinical relevance of OSM in inflammatory diseases: a comprehensive review. Front Immunol 2023;14:1239732. https://doi.org/10.3389/fimmu.2023.1239732.

[30] Aziz A, Soucie E, Sarrazin S, et al. MafB/c-Maf deficiency enables self-renewal of differentiated functional macrophages. Science 2009;326:867-871. https://doi.org/10.1126/science.1176056.

[31] Kikuchi K, Iida M, Ikeda N, et al. Macrophages Switch Their Phenotype by Regulating Maf Expression during Different Phases of Inflammation. J Immunol 2018;201:635-651.

https://doi.org/10.4049/jimmunol.1800040.

Figure legends

Fig. 1. Spatiotemporal heterogeneity of macrophages in mouse and human ICC tissues.(A) (i) UMAP (i) and stacked bar (ii) visualisation of ICC patient TAM subclusters profile (datasets GSE138709 and GSE189903). Malignant (Mal), boundary (Bdy), adjacent non-malignant (nMal). (B) UMAP(i), scatter plot of M2 polarisation scores (ii) and the temporal distribution (iii) of TAM subclusters in AKT1/NICD1 mice. WT (healthy, N=2), D7 (early stage, N=2), D15 (middle stage, N=3), D25 (middle to advanved stage, N=2), D31 (advanced stage, N=3). (C) Bubble plots displaying the expression of TAM marker genes in patients with ICC and the AKT1/NICD1 mice. Color indicates expression levels, bubble size reflects cell proportion. (D) Temporal dynamics of TAM subcluster scores (Mφ_S100a and Mφ_SPP1), red denotes mean expression above the 90th percentile. (E) Scatter–pie plots illustrating prognostic associations of distinct TAM subclusters. Pie chart illustrating cell prognosis outcomes in each TAM subtype. Blue, survival. Red, death. Grey, no significant association.(F) (i)Subcutaneous co-injection tumor model experiments were performed to validate the role of macrophage infiltration in ICC progression. BR group：injection of BR primary cells alone. BR+BMDM group: co-injection of BR primary cells with BMDM. From left to right, representative photographs of xenograft tumors, tumor volume growth curves (in units of 1,000 mm^3), and tumor weights are shown. (ii) In the AKT1/NICD1-driven ICC mouse model, macrophage depletion was achieved via clodronate liposome injection to investigate its impact on ICC progression. The control group received neutral control liposomes. Left: representative liver images . Right: Macrophage infiltration levels (R1, CD11b□F4/80□ cells within CD45□ population; R2, F4/80□ cells within CD11b□ population) analyzed via flow cytometry and correlated with liver-to-body weight ratio using scatter plots. Correlation analysis

was performed using Spearman's rank correlation test. (G) (i) 10X Visium spatial transcriptomics of ICC patient tissue identified seven cell populations.(ii) Scatter plot shows functional regions predicted by Cottrazm (Mal = malignant, Bdy = boundary, nMal = adjacent non malignant).(iii) Stacked bar plots display cell-type proportions across spatial clusters from xCell analysis.(iv) Heatmap shows scaled median cell-type compositions per niche; asterisks denote enrichment in a niche (one-sided Wilcoxon rank sum test, adj. $p < 0.05$). (H) (i)Spatial transcriptomics identified 12 clusters in the BMKMANU S1000 AKT1/NICD1 ICC tissue. Heatmap showing the $CK7^{+}CK19^{+}$ ICC cells (ii) and Mφ_Spp1 (iii) using the RCTD cell type definition. (iv) Contour maps highlighting spatial expression of mean expression of Mφ_Spp1 signature scores. (I) (i) Spatial domains defined by BANKSY in ICC patient dataset using 10X HD platform. (ii) mIF illustrated the spatial distribution of $CD68^{+}$ cells and their distances to $CK19^{+}$ cells. (iii) Cell-type composition across the spatial domains. (iv) Spatial proximity between Mφ_SPP1 and $CK7^{+}CK19^{+}$ cells. (v) Median importance of cell-type abundance in the prediction of abundances of other cell types in the local niche view. (J) (i) Bar plots showing the proportion of $SPP1^{+}CD68^{+}$ cells at different distance bins from $CK19^{+}$ cells in two validation datasets. (ii) Heatmap of tissue spatial infiltration patterns for $CK19^{+}$ cells (highlighted in yellow) in a representative sample. (iii) Zoomed-in view demonstrating dense infiltration of $SPP1^{+}CD68^{+}$ macrophages surrounding $CK19^{+}$ cells.

Fig. 2. Mφ_SPP1 promotes ICC proliferation via OSM-OSMR. (A) UMAP plot (left) and bubble plot (right) illustrating the distribution of epithelial cells in AKT1/NICD1 mice and the cell type features. (B) UMAP plots showing the ICC patients epithelial subtypes. (C) Venn diagram

showing overlap of ligand genes that are significantly upregulated in Mφ_SPP1 which exhibit strong interactions with tumor cells as identified by three cell communication methods (CellphoneDB, CpDB; CellChat, and Niche, NicheNet). (D) Heatmap showing the interaction intensity between TAMs and ICC cells in AKT1/NICD1-mediated *OSM* signalling. (E) Bubble chart visualising pathway enrichment results for downstream target genes of *OSM* in E_Jun (AKT1/NICD1 mouse) and E_CD74 (Human) via NicheNet calculated by clusterprofiler. Schematic of in vivo experimental design (F-i). Representative images (F-ii) of livers from $Lifr^{fl/fl}$ and $Osmr^{fl/fl}$ control mice and $Lifr^{fl/fl}$;Alb-Cre and $Osmr^{fl/fl}$;Alb-Cre mice injected with AKT1/NICD1 and their liver-to-body weight ratios (G). Data are presented as mean ± SD. Statistical significance was analyzed by one-way ANOVA ($p < 0.05$) followed by Dunnett's test (ns, not significant, $^{**}p < 0.01$, $^{***}p < 0.001$; $^{****}p < 0.0001$). (H) Multiplex immunofluorescence showing spatial co-localisation between CD68□OSM□ TAMs and OSMR□KRT19□ ICC cells in ICC patients. Scale bar, 200 μm.

Fig. 3. Mφ_SPP1 promotes ICC proliferation by upregulating p-STAT3 and CCND1 in ICC cells. (A) Bar plot showing gene expression levels in co-culture. Statistical significance was analyzed by one-way ANOVA ($p < 0.05$) followed by Dunnett's test (ns, not significant, $^{**}p < 0.01$, $^{***}p < 0.001$; $^{****}p < 0.0001$). R, Raw264.7. Q, QBC939. (B) CCK-8 assay measuring cell viability of HuCCT1 and QBC939 cells treated with 2.5 ng/mL or 5.0 ng/mL OSM, or left untreated, for 5 consecutive days. (C) (i) EdU incorporation assay in QBC939 cells transduced with control vector or OSMR-targeting sgRNAs (sgOSMR-1, sgOSMR-2). Scale bar, 200 μm. (ii) CCK-8 assay measuring viability of HuCCT1 and QBC939 cells transduced with control vector or

sgOSMR-1 at days 1, 3, and 5 after seeding. (iii) Colony formation assay with crystal violet staining of HuCCT1 and QBC939 cells transduced with control vector or sgOSMR-1. (D) Bar plot showing KEGG pathway enrichment among phosphorylated proteins after OSM treatment in QBC939 cells. Blue, downregulation; Red, upregulation. (E) Network showing OSMR related pathways. H&E staining and IHC staining for OSMR, OSM, CK19, and Ki-67 in paraffin-embedded liver sections(F) and western blot analysis of OSMR, CCND1, BCL2, phosphorylated STAT3 (p-STAT3), phosphorylated mTORC1 (p-mTORC1), and OSM protein levels，GAPDH served as a loading control (G) from $Osmr^{fl/fl}$ and $Osmr^{fl/fl}$; Alb-Cre mice injected with AKT1/NICD1. Scale bar, 200 μm. Data are presented as mean ± SD. Significance was determined by two-tailed unpaired t-test (***$p < 0.001$) for B and C.

Fig. 4. Mφ_SPP1 promotes ICC invasion via *THBS1-CD47* signaling. (A) (i) Heatmap of interactions between TAMs and tumor subtypes in THBS1 signaling. Sender,ligand source. Receiver, receptor. Color intensity indicates importance. (ii) Top, bar plot showing receive contributions of ligand THBS1. Bottom row shows *Cd47* expression across AKT1/NICD1 epithelial subclusters. (iii) Spatial patterns of *THBS1-CD47* interaction. (B) Bubble chart visualising pathway enrichment for downstream target genes of *THBS1* in E_Jun (AKT1/NICD1 mouse) and E_IGFBP7 (Human) via NicheNet. Bubble size depicts enrichment score and colour showcasing significance (-log10(p.adj), clusterProfiler). (C) Representative scratch□wound images of HuCCT1 and RBE cells with or without 10 ng/mL THBS1 or control. HuCCT1 at 0, 12 and 24 h; RBE at 0, 36 and 72 h. Scale bar, 150 μm. (D) Representative crystal violet–stained Transwell migration images of primary BR cells and HuCCT1 cells treated with 10 ng/mL THBS1

or control. Scale bar, 150 μm. (E) qRT-PCR analysis of *CD47* levels in HuCCT1 cells transfected with siScramble control, siCD47-1, or siCD47-2 for 48 h. Data are presented as mean ± SD. Statistical significance was analyzed by one-way ANOVA ($p < 0.05$) followed by Dunnett's test (****$p < 0.0001$).(F) Representative crystal violet–stained Transwell migration images of HuCCT1 cells transfected with siScramble or siCD47-2. Scale bar, 150 μm. (G) qRT-PCR (i) and western blot (ii) analyses of CD47 transcript and protein levels, respectively, in BR cells transduced with LV3-shNC control lentivirus or LV3-shCD47. (H) EdU incorporation assay assessing proliferation of BR cells transduced with LV3-shNC or LV3-shCD47 lentivirus. Scale bar, 50 μm. (I) Colony formation assay comparing BR cells transduced with LV3-shNC or LV3-shCd47 lentivirus. (J) CCK-8 assay measuring cell growth of BR cells transduced with LV3-shNC or LV3-shCd47 lentivirus from day 1 to day 5 after seeding. (K) Representative crystal violet–stained Transwell migration images and corresponding chamber images of BR cells transduced with LV3-shNC or LV3-shCd47 co-cultured with BMDMs or cultured with complete medium for 24 h. Scale bar, 150 μm. (L) Subcutaneous allograft ICC growth curves and representative ICC tissue images (i) of BR cells transduced with LV3-shNC or LV3-shCd47 lentivirus (ii). (M) Representative images of mouse abdominal phenotypes at tumor endpoint after intraperitoneal injection of BR cells transduced with LV3-shNC or LV3-shCd47; tumor sites indicated by white arrows; quantification of metastatic nodules and volume of ascites collected. Data are presented as mean ± SD. Significance was determined by two-tailed unpaired t-test (***$p < 0.001$) for E, G, J and L.

Fig. 5. Mφ_SPP1 promotes ICC invasion via mTOR-mediated phosphorylation of DBN1. (A)

Western blotting showing the expression of p-mTOR, p-RPS6, EpCAM, N-cadherin, Vimentin, and the internal control GAPDH in HuCCT1 cells after THBS1 protein stimulation. (B) Bar plot displaying pathway enrichment analysis for HuCCT1 at 6 h and 2 h following the addition of exogenous THBS1 protein. (C) Circos plot displaying differentially phosphorylated sites at multiple time points after adding exogenous THBS1. From inner to outer rings: phosphorylation-site proportions, phosphopeptide expression intensity (inner heatmap), sample groups, and enriched signaling pathways; the outermost ring lists gene symbols and phosphosites unique to each treatment. Colored links show shared phosphosites-gray, common to control and treatments. Brown, mTOR-related. Red, fibrosis-related. Green, mesenchymal-related. Large and small ticks denote 50 and 5 phosphopeptides, respectively. (D) Western blot analysis of DBN1, phosphorylated DBN1 (p-DBN1), and Vimentin protein levels in BR cells cultured alone or co-cultured with BMDMs for 24 h or 48 h; GAPDH served as a loading control. (E) Representative crystal violet–stained images from Transwell migration assays of HuCCT1 and BR cells co-cultured with BMDMs, with or without Rapamycin treatment. N = 5. Scale bar, 200 μm. (F) Representative crystal violet–stained images from Transwell migration assays of HuCCT1 and BR cells treated with THBS1, with or without Rapamycin blockade; groups include control, THBS1 treatment, and THBS1 combined with Rapamycin. N = 5. Scale bar, 200 μm. (G) Representative chamber and crystal violet–stained images of Transwell migration assays for HuCCT1 cells (i) treated with 0, 5, 25, and 125 μM BTP2 inhibitor, and BR cells (ii) treated with 0, 25, and 125 μM BTP2 in the lower chamber. Scale bar, 200 μm. (H) Representative images of metastatic ICC lesions from various organs in $Thbs1^{fl/fl}$;Lyz-Cre and $Thbs1^{fl/fl}$ mice injected with sgP19/KRAS. Scale bars: 1 cm for liver; 5 mm for lung, spleen, kidney, peritoneum, and colon. (I).

H&E, CK19, and Ki67 staining of metastatic tumor nests in sections from different organs in Thbs1$^{fl/fl}$;Lyz-Cre and Thbs1$^{fl/fl}$ mice injected with sgP19/KRAS. This lymph node is referred to the largest lymph node adjacent to the spleen. Scale bar, 200 μm. (J) Western blot analysis of DBN1, CD47, p-mTORC1(Ser2448), and Vimentin protein expression in tumor tissues from Thbs1$^{fl/fl}$;Lyz-Cre and Thbs1$^{fl/fl}$ mice injected with sgP19/KRAS; GAPDH served as loading control. (K) Representative images of liver phenotypes and quantification of liver-to-body weight ratios in Thbs1$^{fl/fl}$;Lyz-Cre and Thbs1$^{fl/fl}$ mice injected with AKT1/NICD1. Data are presented as mean ± SD. Significance was determined by two-tailed unpaired t-test (*p < 0.05), N = 6. (L) H&E staining of liver sections showing whole-slide and magnified tumor areas in Thbs1$^{fl/fl}$;Lyz-Cre and Thbs1$^{fl/fl}$ mice injected with AKT1/NICD1. Scale bar, 100 μm. (M) Western blot analysis of THBS1, CD47, DBN1, p-DBN1(ser142), p-mTORC1(Ser2448), and Vimentin protein expression in tumor tissues from Thbs1$^{fl/fl}$;Lyz-Cre and Thbs1$^{fl/fl}$ mice injected with AKT1/NICD1; GAPDH served as loading control. AN, AKT1/NICD1.

Fig. 6. Combined intervertion with OSM inhibitor and THBS1 knockout effectively delays ICC progression. (A) Stacked bar plot illustrating the prevalence of OSM□THBS1□ dual-positive patients within distinct ICC cohorts. (B) High (red) and low (green) groups were defined by the mean expression of OSM and THBS1 respectively; survival in three datasets was compared using the log□rank test. (C) Representative liver phenotype images from four experimental groups in the *THBS1/OSM* combination blockade experiment: (1) Thbs1$^{fl/fl}$ + vehicle control; (2) Thbs1$^{fl/fl}$ + OSM-SMI-10B; (3) Thbs1$^{fl/fl}$; Lyz2-Cre + vehicle control; (4) Thbs1$^{fl/fl}$; Lyz2-Cre + OSM-SMI-10B. (C) Statistical analysis of liver-to-body weight ratio across

different treatment groups in the *THBS1/OSM* combination blockade experiment. Data are presented as mean ± SD. Statistical significance was analysed by one-way ANOVA ($p < 0.05$) followed by Dunnett's test (*$p < 0.05$, **$p < 0.01$, ***$p < 0.001$; ****$p < 0.0001$). (D) H&E and IHC staining of liver sections from the *THBS1/OSM* combination blockade experiment. Ki67 and Ck19 positively identifies ICC tumor nest regions. Scale bar, 200 μm. (F) (i) Proximity of $OSM^+THBS1^+CD68^+SPP1^+$ cells to $CK19^+$ cells by mIF. yellow, $CK19^+$; orange□red/green/blue, 0–20, 20–40, 40–60 μm from $CK19^+$. (ii) mIF shows $OSM^+THBS1^+CD68^+SPP1^+$ macrophages around $CK19^+$ cells. (iii) Spearman correlation between OSM/THBS1 and CD68. (iv) Patients stratified by OSM/THBS1 intensity (red = high, green = low); survival compared by log□rank test.

Fig. 7. Epigenetic regulatory profile of ICC TAM subtypes and key regulators in Mφ_SPP1. (A) (i) UMAP of major subtypes identified by scATAC-seq in AKT1/NICD1. (ii) Chromatin accessibility of representative marker genes for each cell type. (B) Volcano plot showing differences in motif deviation scores (chromVAR) between Mφ_S100a and Mφ_SPP1 macrophage subclusters. X-axis: mean motif difference; Y-axis: -log10(FDR). Red dots mark the top 10 transcription factors with the largest accessibility changes (mean difference > 0.05, FDR < 0.05; Wilcoxon test in ArchR). (C) (i) Venn diagram showing transcription factors with the most distinct motifs between the two subclusters and their overlap with factors expressed >1. (ii) UMAP scatter plots depicting chromatin accessibility distribution for representative differential motifs. (D) Bubble plots depicting pathway enrichment of putative target genes regulated by transcription factors *Klf3* in Mφ_S100a(i) and *Mafb* in Mφ_SPP1(ii). (E) Spatial expression patterns of the key transcription factor *MAFB* in AKT1/NICD1 mice and human tissues. (F)

qRT-PCR analysis of *Tgfbr2*, *Mafb*, *Thbs1*, and *Osm* after BMDM polarising with TCM for 2, 6, 12, 24, 36, and 48 hours. (G) qRT-PCR evaluating *Tgfbr2*, *Mafb*, *Thbs1*, and *Osm* transcript levels under different culture conditions. (H) qRT-PCR analysis of *Arg1*, *Vegfa*, *Osm*, and *Thbs1* in siScramble non-polarised, siScramble TCM polarised, and siMafb-1 or siMafb-2 TCM treated groups. Data are presented as mean ± SD. Statistical significance was analysed by one-way ANOVA ($p < 0.05$) followed by Dunnett's t-test (*$p < 0.05$, **$p < 0.01$, ***$p < 0.001$; ****$p < 0.0001$) for F, G and H.

771

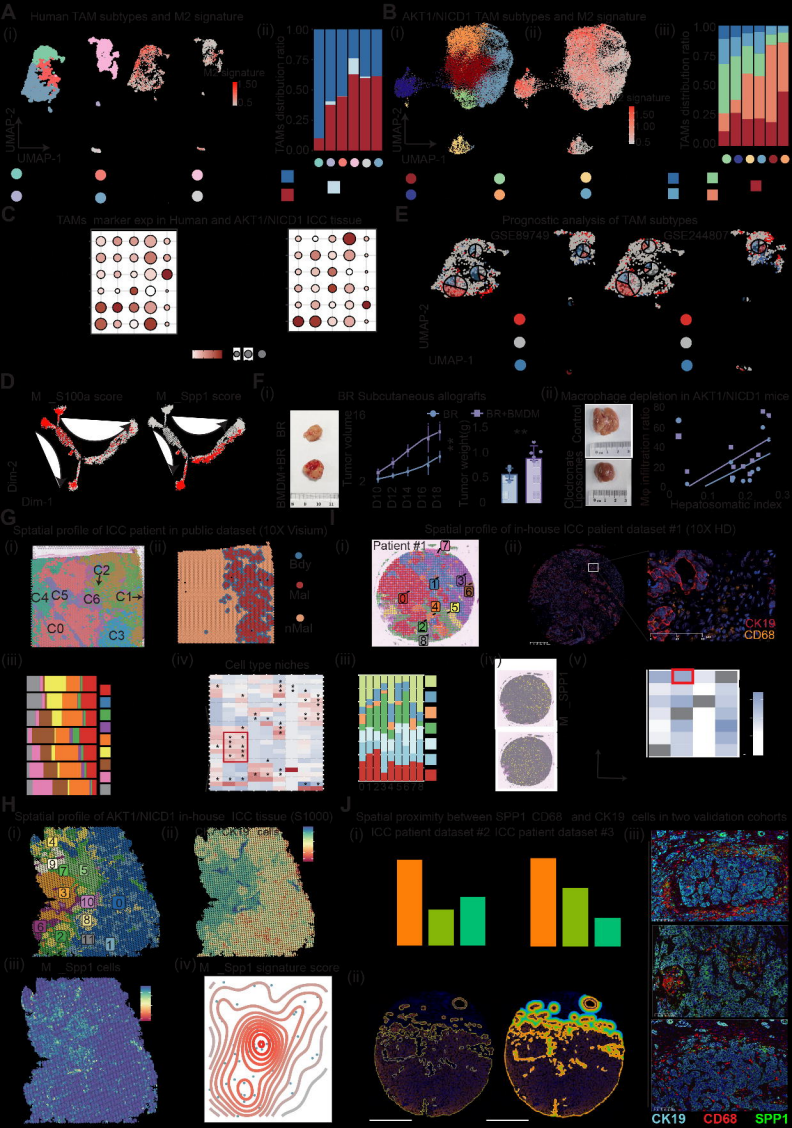
A
Human TAM subtypes and M2 signature
(i)
(ii)
(iii)
UMAP-2
UMAP-1
M2 signature
1.50
0.5
TAMs distribution ratio
1.00
0.75
0.50
0.25
0.00
B
AKT1/NICD1 TAM subtypes and M2 signature
C
TAMs marker exp in Human and AKT1/NICD1 ICC tissue
E
Prognostic analysis of TAM subtypes
GSE89745
GSE244807
D
M_S100a score
M_Spp1 score
Dim-2
Dim-1
F
(i)
BR Subcutaneous allografts
BR
BR+BMDM
Tumor weight(g)
D10
D12
D14
D16
D18
**
(ii)
Macrophage depletion in AKT1/NICD1 mice
Clodronate
Control
Hepatosomatic index
G
Spatial profile of ICC patient in public dataset (10X Visium)
C2
C4
C5
C6
C1
C0
C3
Bdy
Mal
nMal
Cell type niches
H
Spatial profile of AKT1/NICD1 in-house ICC tissue (S1000)
M_Spp1 cells
M_Spp1 signature score
I
Spatial profile of in-house ICC patient dataset #1 (10X HD)
Patient #1
CK19
CD68
M_SPP1
J
Spatial proximity between SPP1, CD68 and CK19 cells in two validation cohorts
ICC patient dataset #2
ICC patient dataset #3
CK19
CD68
SPP1

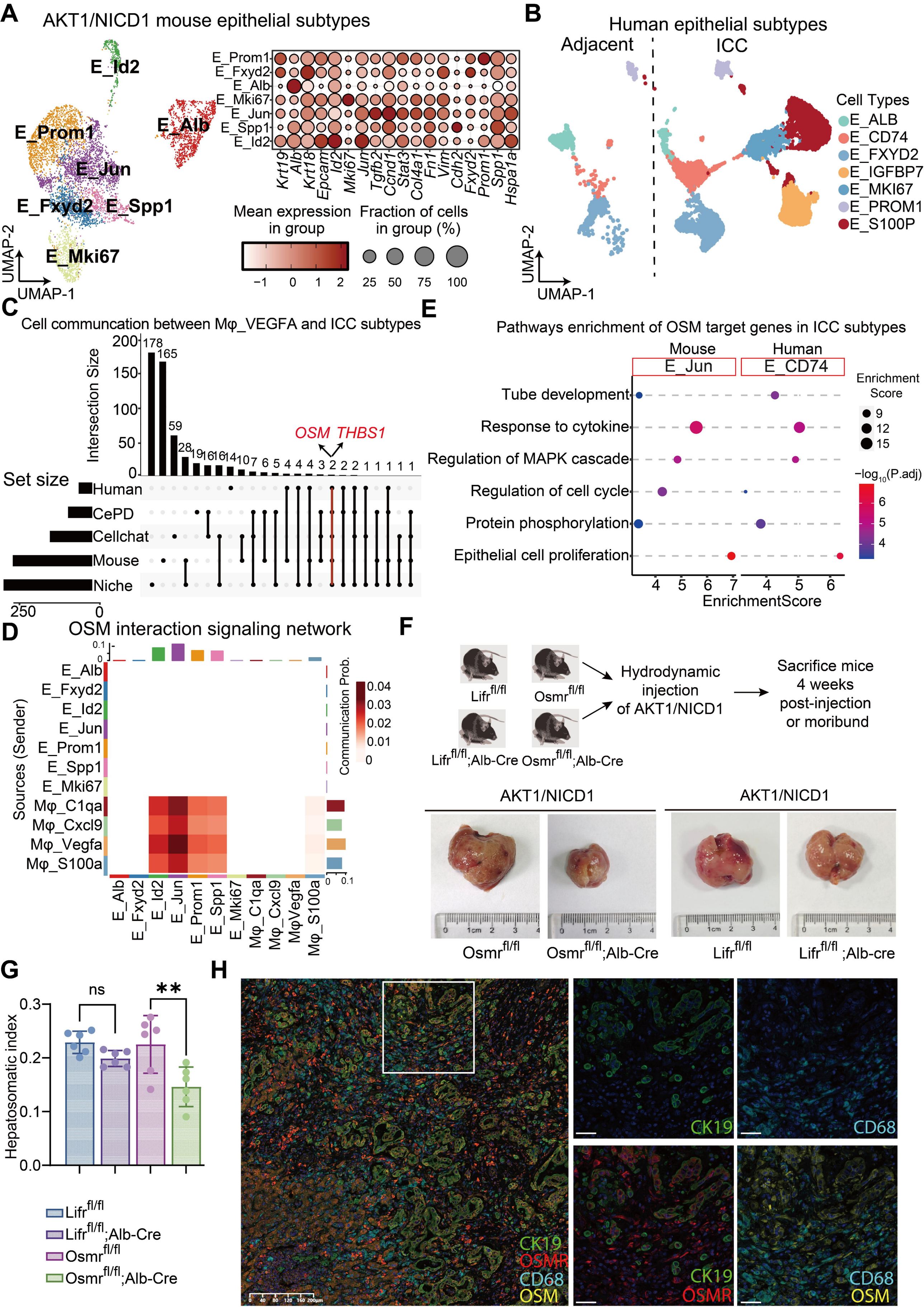
A
AKT1/NICD1 mouse epithelial subtypes
E_Id2
E_Prom1
E_Alb
E_Jun
E_Fxyd2
E_Spp1
E_Mki67
UMAP-2
UMAP-1
E_Prom1
E_Fxyd2
E_Alb
E_Mki67
E_Jun
E_Spp1
E_Id2
Krt19
Alb
Krt18
Epcam
Id2
Mki67
Jun
Tgfb2
Ccnd1
Stat3
Col4a1
Fn1
Vim
Cdh2
Fxyd2
Prom1
Spp1
Hspa1a
Mean expression in group
Fraction of cells in group (%)
−1 0 1 2
25 50 75 100
B
Human epithelial subtypes
Adjacent
ICC
Cell Types
E_ALB
E_CD74
E_FXYD2
E_IGFBP7
E_MKI67
E_PROM1
E_S100P
UMAP-2
UMAP-1
C
Cell communcation between Mφ_VEGFA and ICC subtypes
Intersection Size
200
150
100
50
0
178
165
59
28
19
16
16
14
10
7
6
5
4
4
4
3
2
2
2
1
1
1
1
1
OSM THBS1
Set size
Human
CePD
Cellchat
Mouse
Niche
250
0
E
Pathways enrichment of OSM target genes in ICC subtypes
Mouse
Human
E_Jun
E_CD74
Tube development
Response to cytokine
Regulation of MAPK cascade
Regulation of cell cycle
Protein phosphorylation
Epithelial cell proliferation
4 5 6 7
4 5 6
EnrichmentScore
Enrichment Score
9
12
15
−log10(P.adj)
6
5
4
D
OSM interaction signaling network
0.1
0
Sources (Sender)
E_Alb
E_Fxyd2
E_Id2
E_Jun
E_Prom1
E_Spp1
E_Mki67
Mφ_C1qa
Mφ_Cxcl9
Mφ_Vegfa
Mφ_S100a
Communication Prob.
0.04
0.03
0.02
0.01
0
F
Lifr fl/fl
Osmr fl/fl
Lifr fl/fl;Alb-Cre
Osmr fl/fl;Alb-Cre
Hydrodynamic injection of AKT1/NICD1
Sacrifice mice 4 weeks post-injection or moribund
AKT1/NICD1
AKT1/NICD1
Osmr fl/fl
Osmr fl/fl;Alb-Cre
Lifr fl/fl
Lifr fl/fl ;Alb-cre
G
ns
**
Hepatosomatic index
0.3
0.2
0.1
0.0
Lifr fl/fl
Lifr fl/fl;Alb-Cre
Osmr fl/fl
Osmr fl/fl;Alb-Cre
H
CK19
OSMR
CD68
OSM
CK19
CD68
CK19
OSMR
CD68
OSM

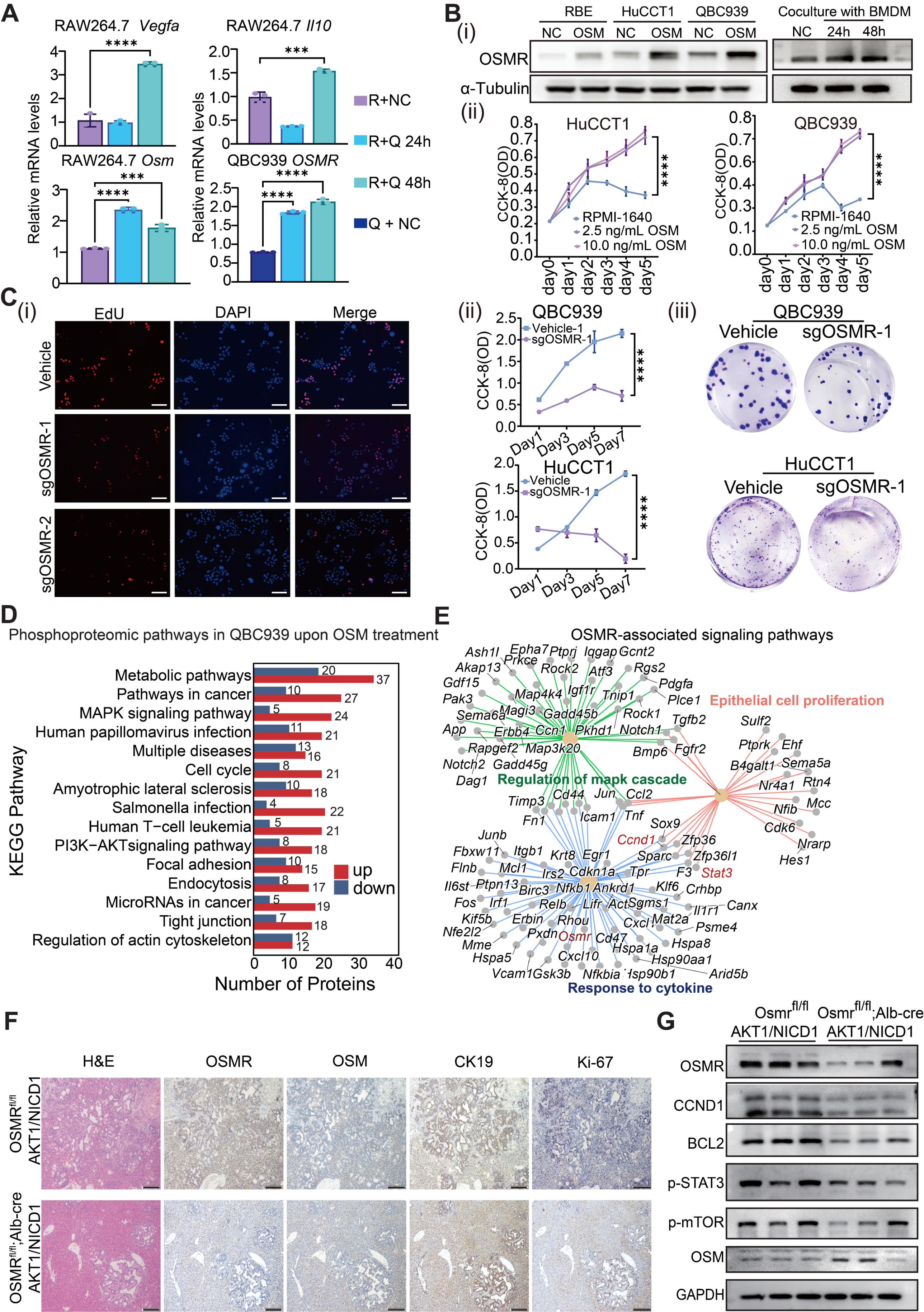
A
RAW264.7 Vegfa
RAW264.7 Il10
RAW264.7 Osm
QBC939 OSMR
Relative mRNA levels
R+NC
R+Q 24h
R+Q 48h
Q + NC
B
(i)
RBE
HuCCT1
QBC939
Coculture with BMDM
NC
OSM
24h
48h
OSMR
α-Tubulin
(ii)
HuCCT1
QBC939
CCK-8(OD)
RPMI-1640
2.5 ng/mL OSM
10.0 ng/mL OSM
(iii)
Vehicle
sgOSMR-1
C
(i)
EdU
DAPI
Merge
Vehicle
sgOSMR-1
sgOSMR-2
(ii)
Day1
Day3
Day5
Day7
D
Phosphoproteomic pathways in QBC939 upon OSM treatment
Metabolic pathways
Pathways in cancer
MAPK signaling pathway
Human papillomavirus infection
Multiple diseases
Cell cycle
Amyotrophic lateral sclerosis
Salmonella infection
Human T−cell leukemia
PI3K−AKTsignaling pathway
Focal adhesion
Endocytosis
MicroRNAs in cancer
Tight junction
Regulation of actin cytoskeleton
KEGG Pathway
Number of Proteins
up
down
E
OSMR-associated signaling pathways
Epithelial cell proliferation
Regulation of mapk cascade
Response to cytokine
F
H&E
OSMR
OSM
CK19
Ki-67
OSMR fl/fl AKT1/NICD1
OSMR fl/fl;Alb-cre AKT1/NICD1
G
Osmr fl/fl
Osmr fl/fl;Alb-cre
AKT1/NICD1
OSMR
CCND1
BCL2
p-STAT3
p-mTOR
OSM
GAPDH

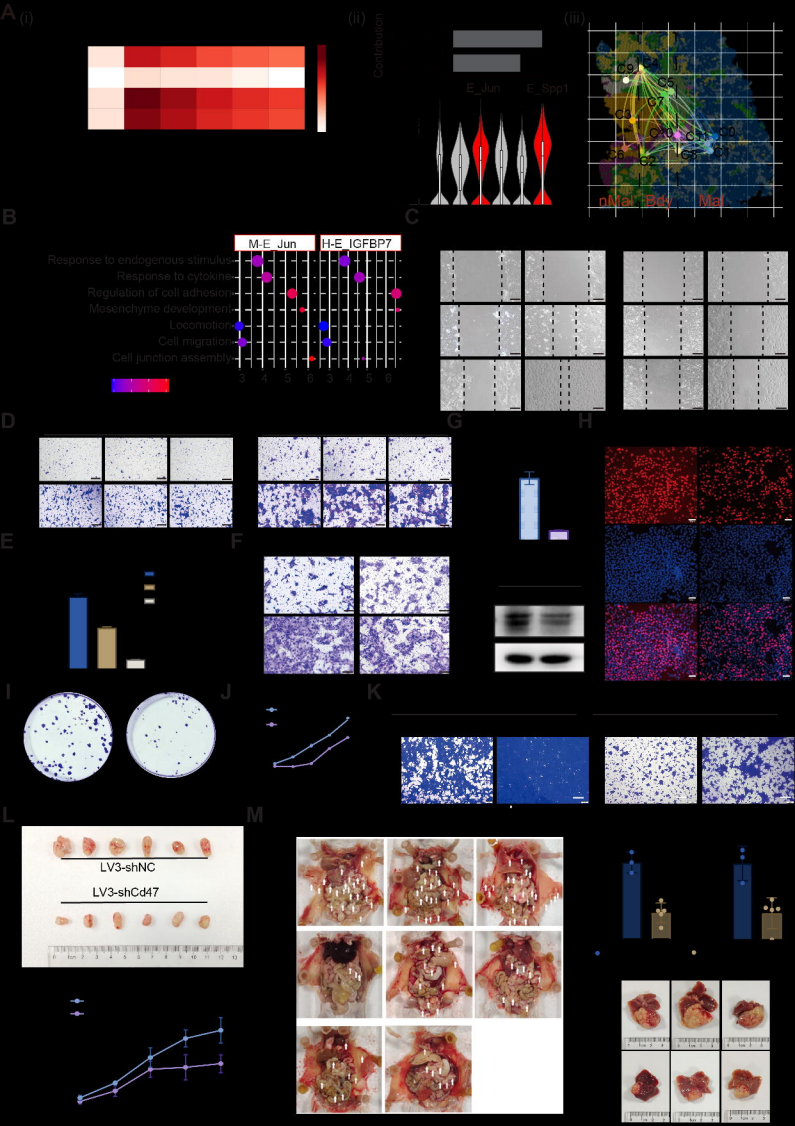
A
(i)
(ii)
Contribution
E_Jun
E_Spp1
(iii)
C1
C2
C3
C4
C5
C6
C7
C8
C9
C10
C11
C0
nMal
Bdy
Mal
B
M-E_Jun
H-E_IGFBP7
Response to endogenous stimulus
Response to cytokine
Regulation of cell adhesion
Mesenchyme development
Locomotion
Cell migration
Cell junction assembly
3 4 5 6 3 4 5 6
C
D
G
H
E
F
I
J
K
L
M
LV3-shNC
LV3-shCd47

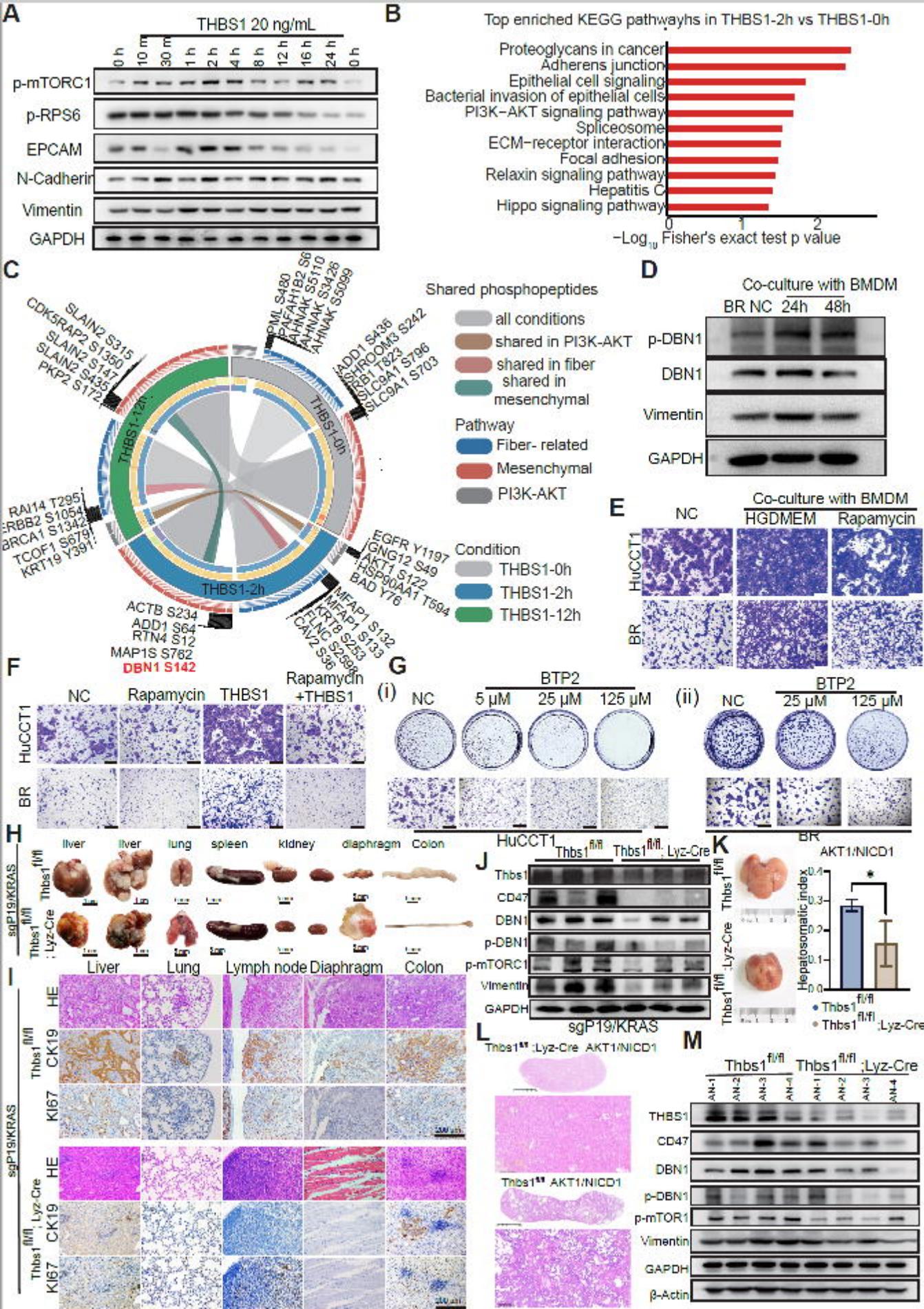
A
THBS1 20 ng/mL
0 h
10 m
30 m
1 h
2 h
4 h
8 h
12 h
16 h
24 h
0 h
p-mTORC1
p-RPS6
EPCAM
N-Cadherin
Vimentin
GAPDH
B
Top enriched KEGG pathwayhs in THBS1-2h vs THBS1-0h
Proteoglycans in cancer
Adherens junction
Epithelial cell signaling
Bacterial invasion of epithelial cells
PI3K−AKT signaling pathway
Spliceosome
ECM−receptor interaction
Focal adhesion
Relaxin signaling pathway
Hepatitis C
Hippo signaling pathway
0
1
2
−Log10 Fisher's exact test p value
C
Shared phosphopeptides
all conditions
shared in PI3K-AKT
shared in fiber
shared in mesenchymal
Pathway
Fiber- related
Mesenchymal
PI3K-AKT
Condition
THBS1-0h
THBS1-2h
THBS1-12h
THBS1-12h
THBS1-0h
THBS1-2h
DBN1 S142
D
Co-culture with BMDM
BR NC
24h
48h
p-DBN1
DBN1
Vimentin
GAPDH
E
Co-culture with BMDM
NC
HGDMEM
Rapamycin
HuCCT1
BR
F
NC
Rapamycin
THBS1
Rapamycin +THBS1
HuCCT1
BR
G
(i)
NC
BTP2
5 μM
25 μM
125 μM
(ii)
NC
BTP2
25 μM
125 μM
HuCCT1
BR
H
liver
liver
lung
spleen
kidney
diaphragm
Colon
sgP19/KRAS
Thbs1fl/fl
Thbs1fl/fl ;Lyz-Cre
I
Liver
Lung
Lymph node
Diaphragm
Colon
HE
CK19
KI67
sgP19/KRAS
Thbs1fl/fl
Thbs1fl/fl ;Lyz-Cre
J
Thbs1fl/fl
Thbs1fl/fl ;Lyz-Cre
Thbs1
CD47
DBN1
p-DBN1
p-mTORC1
Vimentin
GAPDH
K
AKT1/NICD1
Hepatosomatic index
Thbs1fl/fl
Thbs1fl/fl ;Lyz-Cre
L
sgP19/KRAS
Thbs1fl/fl ;Lyz-Cre AKT1/NICD1
Thbs1fl/fl AKT1/NICD1
M
Thbs1fl/fl
Thbs1fl/fl ;Lyz-Cre
AN-1
AN-2
AN-3
AN-4
THBS1
CD47
DBN1
p-DBN1
p-mTOR1
Vimentin
GAPDH
β-Actin

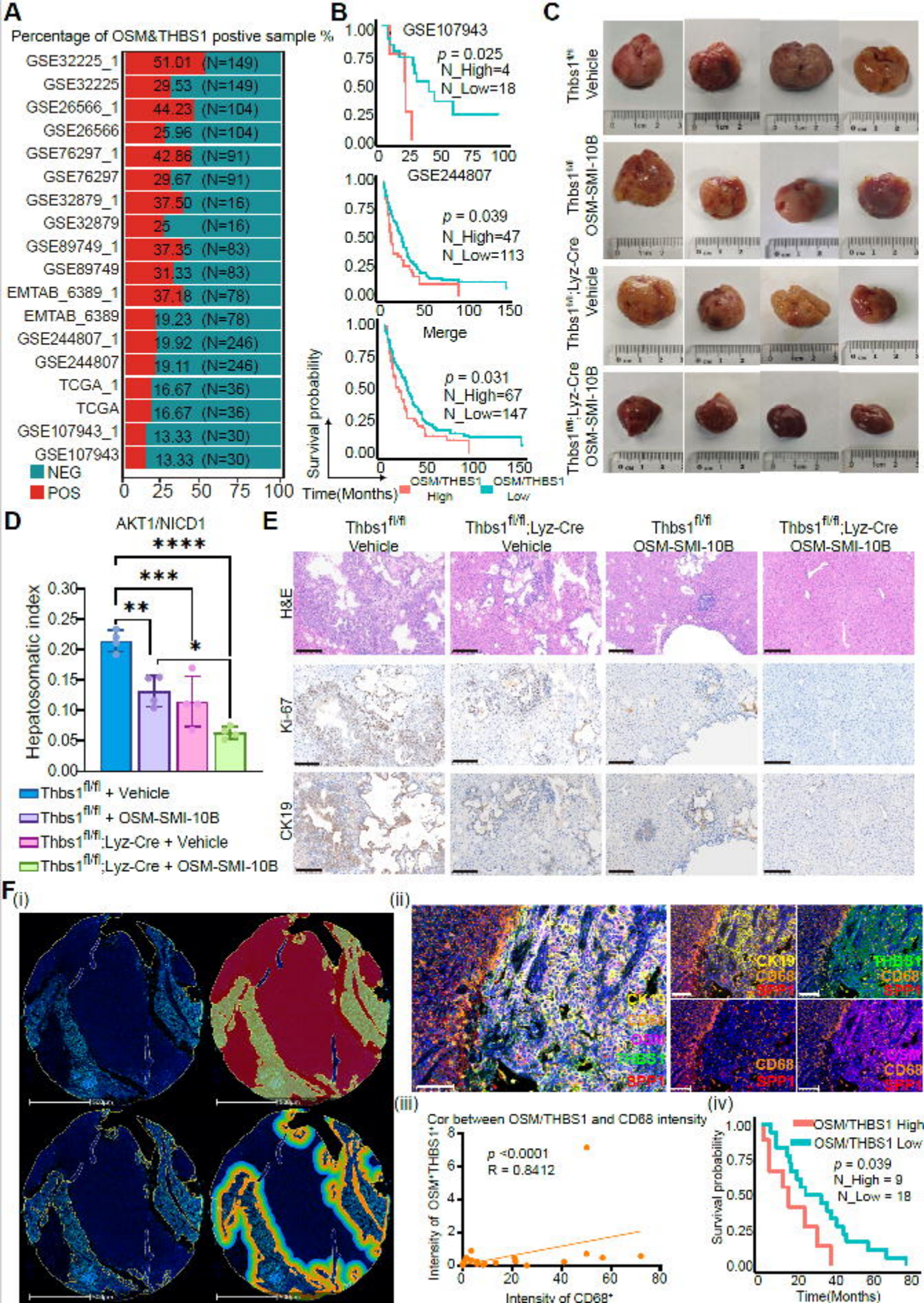
A
Percentage of OSM&THBS1 postive sample %
GSE32225_1 51.01 (N=149)
GSE32225 29.53 (N=149)
GSE26566_1 44.23 (N=104)
GSE26566 25.96 (N=104)
GSE76297_1 42.86 (N=91)
GSE76297 29.67 (N=91)
GSE32879_1 37.50 (N=16)
GSE32879 25 (N=16)
GSE89749_1 37.35 (N=83)
GSE89749 31.33 (N=83)
EMTAB_6389_1 37.18 (N=78)
EMTAB_6389 19.23 (N=78)
GSE244807_1 19.92 (N=246)
GSE244807 19.11 (N=246)
TCGA_1 16.67 (N=36)
TCGA 16.67 (N=36)
GSE107943_1 13.33 (N=30)
GSE107943 13.33 (N=30)
NEG
POS
B
GSE107943
p = 0.025
N_High=4
N_Low=18
GSE244807
p = 0.039
N_High=47
N_Low=113
Merge
p = 0.031
N_High=67
N_Low=147
Survival probability
Time(Months)
OSM/THBS1 High
OSM/THBS1 Low
C
Thbs1fl/fl Vehicle
Thbs1fl/fl OSM-SMI-10B
Thbs1fl/fl;Lyz-Cre Vehicle
Thbs1fl/fl;Lyz-Cre OSM-SMI-10B
D
AKT1/NICD1
Hepatosomatic index
Thbs1fl/fl + Vehicle
Thbs1fl/fl + OSM-SMI-10B
Thbs1fl/fl;Lyz-Cre + Vehicle
Thbs1fl/fl;Lyz-Cre + OSM-SMI-10B
E
Thbs1fl/fl Vehicle
Thbs1fl/fl;Lyz-Cre Vehicle
Thbs1fl/fl OSM-SMI-10B
Thbs1fl/fl;Lyz-Cre OSM-SMI-10B
H&E
Ki-67
CK19
F
(i)
(ii)
CK19
CD68
OSM
THBS1
SPP1
(iii)
Cor between OSM/THBS1 and CD68 intensity
p <0.0001
R = 0.8412
Intensity of OSM+THBS1+
Intensity of CD68+
(iv)
OSM/THBS1 High
OSM/THBS1 Low
p = 0.039
N_High = 9
N_Low = 18
Survival probability
Time(Months)

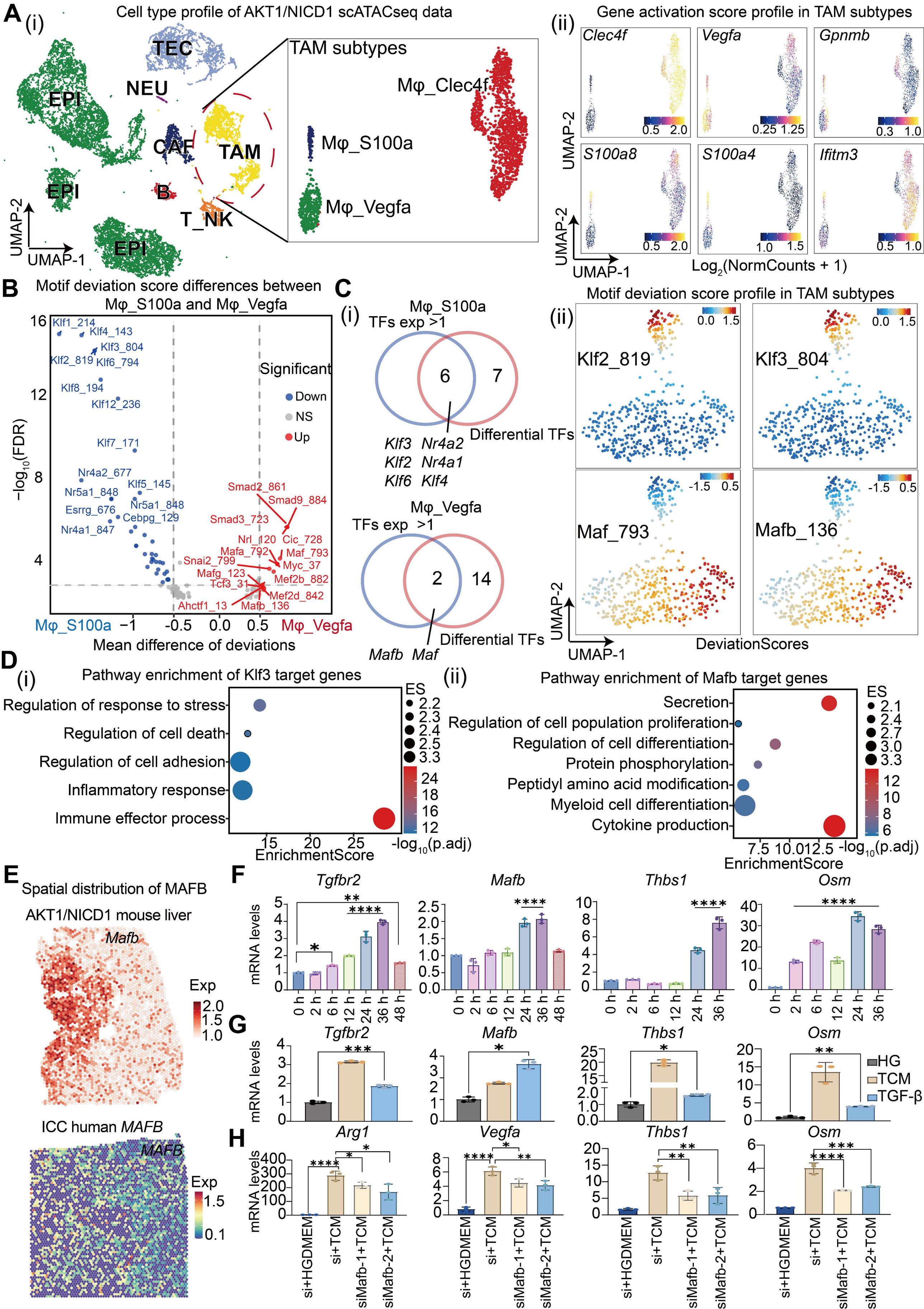
A
(i)
Cell type profile of AKT1/NICD1 scATACseq data
TEC
NEU
EPI
CAF
TAM
B
T_NK
UMAP-2
UMAP-1
TAM subtypes
Mφ_Clec4f
Mφ_S100a
Mφ_Vegfa
(ii)
Gene activation score profile in TAM subtypes
Clec4f
Vegfa
Gpnmb
S100a8
S100a4
Ifitm3
Log2(NormCounts + 1)
B
Motif deviation score differences between Mφ_S100a and Mφ_Vegfa
−log10(FDR)
Significant
Down
NS
Up
Klf1_214
Klf4_143
Klf3_804
Klf2_819
Klf6_794
Klf8_194
Klf12_236
Klf7_171
Nr4a2_677
Klf5_145
Nr5a1_848
Esrrg_676
Cebpg_129
Nr4a1_847
Smad2_861
Smad9_884
Smad3_723
Nrl_120
Cic_728
Mafa_792
Maf_793
Snai2_799
Myc_37
Mafg_123
Mef2b_882
Tcf3_31
Mef2d_842
Ahctf1_13
Mafb_136
Mφ_S100a
Mφ_Vegfa
Mean difference of deviations
C
(i)
Mφ_S100a
TFs exp >1
6
7
Differential TFs
Klf3 Nr4a2
Klf2 Nr4a1
Klf6 Klf4
Mφ_Vegfa
TFs exp >1
2
14
Differential TFs
Mafb Maf
(ii)
Motif deviation score profile in TAM subtypes
Klf2_819
Klf3_804
Maf_793
Mafb_136
DeviationScores
D
(i)
Pathway enrichment of Klf3 target genes
Regulation of response to stress
Regulation of cell death
Regulation of cell adhesion
Inflammatory response
Immune effector process
ES
EnrichmentScore
-log10(p.adj)
(ii)
Pathway enrichment of Mafb target genes
Secretion
Regulation of cell population proliferation
Regulation of cell differentiation
Protein phosphorylation
Peptidyl amino acid modification
Myeloid cell differentiation
Cytokine production
E
Spatial distribution of MAFB
AKT1/NICD1 mouse liver
Mafb
Exp
ICC human MAFB
MAFB
F
Tgfbr2
Mafb
Thbs1
Osm
mRNA levels
0 h
2 h
6 h
12 h
24 h
36 h
48 h
G
HG
TCM
TGF-β
H
Arg1
Vegfa
si+HGDMEM
si+TCM
siMafb-1+TCM
siMafb-2+TCM